Probability law of turbulent kinetic energy in the atmospheric surface layer

Mohammad Allouche,[1,*] Gabriel G. Katul,[2,3,1] Jose D. Fuentes,[4] and Elie Bou-Zeid[1]
[1]*Department of Civil and Environmental Engineering, Princeton University, Princeton, New Jersey 08544, USA*
[2]*Nicholas School of the Environment, Box 80328, Duke University, Durham, North Carolina 27708, USA*
[3]*Department of Civil and Environmental Engineering, Duke University, Durham, North Carolina 27708, USA*
[4]*Department of Meteorology and Atmospheric Sciences, Penn State University, Pennsylvania 16801, USA*

(Received 16 June 2020; accepted 8 June 2021; published 1 July 2021)

The probability density function $p(k)$ of the turbulent kinetic energy k is investigated for diabatic atmospheric surface layer (ASL) flows. When the velocity components are near-Gaussian and their squared amplitudes are nearly independent, the resulting $p(k)$ is shown to be γ-distributed with exponents that vary from 0.8 to 1.8. A nonlinear Langevin equation that preserves a γ-distributed $p(k)$, but allows linear relaxation of k to its mean state, is proposed and tested using multiple ASL data sets. The three parameters needed to describe the drift and nonlinear diffusion terms can be determined from the ground shear stress and the mean velocity at height z. Using these model parameters, the Langevin equation reproduces the measured $p(k)$ with minimal Kullback-Leibler divergence.

DOI: 10.1103/PhysRevFluids.6.074601

I. INTRODUCTION

The significance of turbulent kinetic energy (TKE) and its variations in the atmospheric surface layer (ASL) is rarely in dispute given its relevance to a plethora of applications. Descriptions of the mean TKE are required in wind energy applications [1], dispersion of pollutants [2], eddy-viscosity formulations for weather forecasts and climate models [3–5], seed or pollen dislodging and spread [6–8], among others. Over the past 2 decades, variability in TKE has also gained attention in studies linking turbulence and super-statistics given the connections to nonextensive entropy measures [9–11]. However, the geophysical and engineering turbulence literature has been rather silent on models and theories describing excursions in TKE from their mean state, despite the wide set of experimental analyses focusing on turbulence intermittency [12–22]. This knowledge gap motivates the present paper.

The instantaneous (k) and mean ($\overline{k}$) TKE are defined as

$$k = \tfrac{1}{2}(u_i' u_i'); \quad \overline{k} = \tfrac{1}{2}(\overline{u_i' u_i'}), \tag{1}$$

where $u_1 = u$, $u_2 = v$, and $u_3 = w$ are the longitudinal, lateral, and vertical components of the velocity aligned along $x_1 = x$, $x_2 = y$, and $x_3 = z$, respectively, with x_3 or z being the distance from the surface or zero-plane displacement. Primed quantities are turbulent quantities defined as departures from an "ensemble mean." Operationally, these primed quantities are determined as departures from the time-averaged state (hereafter indicated by overbar) as common in field experiments. Meteorological and index notations are used throughout. The budget of $\overline{k}$ has been extensively studied and forms the basis of Monin-Obukhov similarity theory (MOST) in the ASL for stationary and planar homogeneous flow in the absence of subsidence [23]. The $\overline{k}$ is also used in

*allouche@princeton.edu

eddy-viscosity (ν_t) calculations, usually expressed in the form $\nu_t = c_1\sqrt{\bar{k}}l_m$ (where c_1 is a similarity constant and l_m is a mixing length), as reviewed elsewhere [24]. Surprisingly, much less is known about the probability density function of k, hereafter referred to as $p(k)$. What is the probability law describing $p(k)$ in the ASL? How do the parameters of this law vary with boundary conditions (e.g., the atmospheric stability parameter $\zeta = z/L$, where L is the Obukhov length [25])? How can this probability law be used in model simulations of k time series? Answering these three questions frames the scope of the work here.

The derivation of a probabilistic model for $p(k)$ and the dependence of its parameters on ζ are explored using published data sets collected in the ASL across a wide range of heights and ζ, and over two contrasting land-cover types. Data from two field experiments, one over ice in Utqiagvik (Barrow), Alaska [26], and the second over a grass-covered forest clearing at Duke forest near Durham, North Carolina [27], are analyzed in this context. The former site is representative of a canonical ASL where Earth's surface is planar-homogeneous. The latter location is characterized by advective distortions to $\bar{k}$ arising from adjustments as the flow transitions from a forest into the clearing or conversely. The paper begins by deriving the probability law $p(k)$, which then serves as the basis of a Langevin equation model for k that can be employed in simulations and models alike. This Langevin equation is presented from a theoretical and modeling perspectives, where its limitations are further addressed.

II. THEORY

A. Background and definitions

In a near-neutral ASL, the statistics of u_i' do not deviate appreciably from Gaussian [28–31] so that their $p(u_i')$ is given by

$$p(s') = G(s') = \frac{1}{\sqrt{2\pi\sigma_s^2}} \exp\left[-\frac{1}{2}\left(\frac{s'}{\sigma_s}\right)^2\right], \tag{2}$$

where s' is a turbulent flow variable representing velocity excursions (i.e., u', v', or w'), $\sigma_s = (\overline{s's'})^{1/2}$ is the root-mean-squared value of a turbulent flow variable s', and $G(s')$ is the Gaussian distribution of s' used for notational simplicity. When $u_1'^2$, $u_2'^2$, and $u_3'^2$ are independent and are such that $\sigma_u = \sigma_v = \sigma_w$ (i.e., equipartitioning of the energy as expected in isotropic turbulence), it directly follows, after normalizing the latter to unit variance, that the sum of these squared normalized instantaneous variables ($e_n = 2k_n$) must be χ-squared distributed given by

$$p(e_n) = \frac{1}{2^{\alpha/2}\Gamma(\alpha/2)} e_n^{\alpha/2-1} \exp\left(-\frac{1}{2}e_n\right), \tag{3}$$

where α is the number of degrees of freedom (=3). For the ASL, $\sigma_u \neq \sigma_v \neq \sigma_w$ and the anisotropy in energy distribution varies with z and ζ. In addition, with changes in ζ, $G(s')$ may no longer be an acceptable descriptor of $p(u_i')$. Nonetheless, it may still be possible to arrive at a reference shape for $p(k)$ that accommodates some of these departures.

The first step is to derive the distributions of u'^2, v'^2, and w'^2 separately by considering the transformation $r = g(s')$ or its inverse $s' = g^{-1}(r)$. Momentarily, it is assumed that $G(s')$ remains an acceptable descriptor of $p(u_i')$. Here, $r = s'^2$ so that $s' = \pm\sqrt{r}$. Then, $p(r)$ is related to $p(s')$ by

$$p(r) = 2G(s')\left|\frac{ds'}{dr}\right|, \tag{4}$$

where the factor 2 arises due to symmetry considerations. Because $ds'/dr = -(1/2)r^{-1/2}$, it follows that

$$p(r) = \frac{1}{\sigma_s\sqrt{2\pi r}} \exp\left[-\frac{1}{2}\frac{r}{\sigma_s^2}\right]. \tag{5}$$

The χ-squared $p(r)$ becomes evident when noting that $\Gamma(1/2) = \sqrt{\pi}$ and that the mean of each normalized variance is $\alpha = \sigma_s^2 = 1$. In its normalized form with $\sigma_s = 1$, this distribution is a special case of the more general γ distribution given by

$$p(r) = \frac{\beta^\gamma}{\Gamma(\gamma)} r^{\gamma-1} \exp(-\beta r), \tag{6}$$

where the case $\beta = 1/2$ and $\gamma = 3/2$ recovers the χ-squared distribution. It is to be noted that when $\gamma = 1$, $p(r)$ is exponential. The γ distribution in Eq. (6) has a mean of γ/β, variance of γ/β^2, skewness of $2/\sqrt{\gamma}$, and excess Kurtosis of $6/\gamma$, and is hereafter assumed to represent the individual (nonnormalized) velocity components $p(s'^2)$.

B. The basic model

As a first approximation, it is assumed that u'^2, v'^2, and w'^2 are each γ-distributed with their own β_u and γ_u, β_v and γ_v, and β_w and γ_w (instead of χ-squared). Moreover, the squared velocity components are assumed to remain independent even when u' may be correlated with w' due to finite turbulent stresses. It is worth noting that the squares of random correlated variables are much less correlated than the original variables (as illustrated later). What is now sought is the distribution of $2k = u'^2 + v'^2 + w'^2$ knowing that the squared velocity components are each γ distributed.

The Welch-Satterthwaite approximation [32,33] leads to $p(2k)$ that is γ distributed given by

$$p(2k) = \frac{(\beta_k)^{\alpha_k}}{\Gamma(\gamma_k)} (2k)^{\gamma_k - 1} \exp[-\beta_k (2k)], \tag{7}$$

where β_k and γ_k are related to β_u and γ_u, β_v and γ_v, and β_w and γ_w via

$$\nu_k = \beta_u\gamma_u + \beta_v\gamma_v + \beta_w\gamma_w, \quad \gamma_k = \frac{\nu_k^2}{\gamma_u\beta_u^2 + \gamma_v\beta_v^2 + \gamma_w\beta_w^2}, \quad \beta_k = \frac{\gamma_u\beta_u^2 + \gamma_v\beta_v^2 + \gamma_w\beta_w^2}{\nu_k}. \tag{8}$$

The work here explores variations of γ_k and β_k of this composite $p(k)$ in the ASL. It is to be noted that fitting a γ distribution to each squared velocity component, inferring the individual β_u and γ_u, β_v and γ_v, and β_w and γ_w, and then using Eq. (8) to compare this outcome to γ_k and β_k obtained by directly fitting a γ distribution to the k time series, allows an indirect assessment of the assumptions used to arrive at Eq. (7).

C. A Langevin model for *k*

With $p(k)$ being γ distributed and assuming an approximate autocorrelation function $\rho_k(\tau) = \exp(-\tau/\tau_k)$ that decays with a characteristic time τ_k (yet to be determined), a Langevin equation for k can now be formulated and is given by [34]

$$dk = -(k - \bar{k})\frac{dt}{\tau_k} + \sqrt{\left(\frac{2\sigma_*^2 \bar{k} k}{\tau_k}\right)} d\omega, \tag{9}$$

where $d\omega$ is the Wiener increment (with zero mean and variance dt), $\sigma_*^2 = \sigma_k^2/\bar{k}^2$ is the variance of $k/\bar{k}$, and dt is the time step used in the time integration of k. The exponential $\rho_k(\tau)$ here ensures that $\tau_k = \int_0^\infty \rho_k(t')dt'$. The three parameters ($\bar{k}$, σ_k, and τ_k) appearing in Eq. (9) must be externally supplied. Because the Langevin equation is evaluated using both measured and modeled parameters for $\bar{k}$, σ_k, and τ_k, it is convenient to distinguish the version with modeled parameters by writing another Langevin equation given as

$$dk = -(k - \bar{k}_m)\frac{dt}{\tau_m} + \sqrt{\left(\frac{2\sigma_m^2 \bar{k}_m k}{\tau_m}\right)} d\omega. \tag{10}$$

Estimates for $\bar{k}_m$, σ_m, and τ_m are sought from the mean velocity, turbulent shear stress, and ζ.

D. An alternative model

In classical models of turbulence closure (e.g., $k-\epsilon$), the mean turbulent kinetic energy dissipation rate $\overline{\epsilon}$ is related to $\overline{k}$ using $\tau_k \sim \overline{k}/\overline{\epsilon}$, where τ_k is known as the relaxation timescale. When τ_k does not vary appreciably, such a closure may (naively) suggest that $p(k)$ resembles $p(\epsilon)$, which is log-normally distributed. If so, then the alternative model to $p(k)$ is not γ but a log-normal. An associated Langevin model for a log-normal k can be derived as commonly done for ϵ [34,35]. However, the relation between the means of the distributions of k and ϵ does not necessarily constrain the relations of their PDFs. Therefore, whether a γ or log-normal model best represents k in the ASL will be explored using the two data sets featured here.

III. FIELD DATA AND METHODS

As briefly mentioned in the Introduction, data from two field experiments are analyzed. One data set is collected over an ice sheet in Utqiagvik (Barrow), Alaska [26], and the second data set is collected over a grass-covered forest clearing at Duke forest near Durham, North Carolina [27]. The sampling frequency at the Barrow experiment was 10 Hz whereas the sampling frequency at the Duke forest clearing was 56 Hz. The data at the Barrow site were collected at two heights ($z_m = 5.7$ m and 11.6 m), whereas at the Duke forest site, data were acquired only at one height ($z_m = 5.6$ m) from the ground surface. The post-processing involved de-spiking and linear detrending before k statistics were determined.

For the Barrow experiment, de-spiking was conducted as follows: data were separated into 5-min running windows and any measurement value with absolute value larger than six times the corresponding standard deviation in this window was flagged. All flagged variables corresponding to that timestamp were removed and replaced with NaNs so they would not affect the statistics. Double rotation of wind components based on 15-min time averages is applied here only over the Barrow site, the same Barrow period used for Reynolds time-averaging throughout. It is to be noted that $\overline{k}$ is a scalar quantity computed from the trace of the stress tensor and thus is independent of the coordinate system.

Similarly, over the Duke grass site, data were separated into 1-min running windows, and if any fluctuating data point had an absolute value larger than five times the corresponding standard deviation in this current window, all measured variables corresponding to that timestamp were removed and replaced with NaNs. For defining the turbulent fluctuations over Duke, a 20-min averaging period was used.

Non-stationarity was assessed by computing the integral timescale of TKE and comparing it to 60 s. Almost all the selected runs at both sites had integral timescales not exceeding 60 s. In what follows, the instantaneous data were collected from a single block of data, i.e., real-time measurement run, and not aggregated over multiple runs. The standard deviation of TKE is $\sigma_k = \sqrt{\overline{(k-\overline{k})^2}}$. This is the same standard deviation used to define the coefficient of variation $CV_k = \sigma_k/\overline{k}$ discussed later.

IV. RESULTS

The results and discussion are structured to evaluate assumptions and approximations leading to the final outcome of $p(k)$ (i.e., a composite γ) and the associated Langevin form in Eqs. (9) and (10).

A. The statistics of u_i', $u_i'^2$, and k

Figure 1 reports one sample period's measured $p(s'/\sigma_s)$ for $s' = u'$, $s' = v'$, and $s' = w'$ along with a zero mean and unit variance $G(s'/\sigma_s)$ across three atmospheric stability regimes (unstable "top row" $\zeta < 0$, neutral "middle row" $\zeta \approx 0$, stable "bottom row" $\zeta > 0$) at the two different sites (Duke Grass "left column," Barrow Ice "right column"). The velocity components deviate from

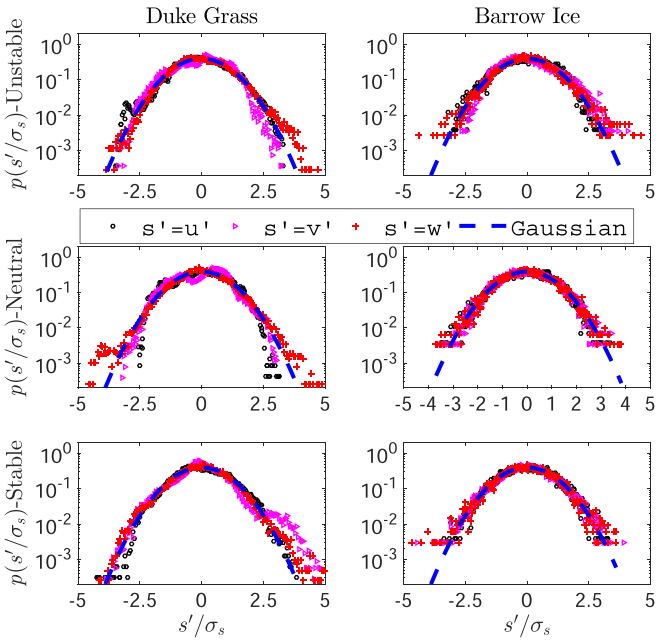

FIG. 1. The probability density function $p(s'/\sigma_s)$ for $s' = u'$, $s' = v'$ and $s' = w'$, with a zero mean and unit variance Gaussian distribution $G(s'/\sigma_s)$ for reference. The measurements are collected at $z_m = 5.1$ m above the grass surface at the Duke Forest, and at $z_m = 5.7$ m and $z_m = 11.6$ m above the ice sheet in Barrow Alaska.

Gaussian, albeit moderately, with u' being more skewed and w' being more intermittent. The derivations for $p(k)$ assumed that the squared velocity components are independent. For a numerical illustration, one run from the Duke Forest site is used as an example. In this run, the correlation coefficient $\rho_{u,w} = -0.34$, whereas $\rho_{u^2,w^2} = 0.08$ and is much smaller in magnitude. That is, while the individual velocity components are significantly correlated, their squared components are much less so. Deviations in the tails from Gaussian are expected at the Duke forest even for near-neutral conditions due to site nonuniformity (unlike the case of Barrow).

Figure 2 shows that the γ distribution describes reasonably the individual normalized velocity components $(u'/\sigma_u)^2$, $(v'/\sigma_v)^2$ and $(w'/\sigma_w)^2$ even though deviations from Gaussian have been noted in Fig. 1. This finding implies that the γ distribution is a robust model for the energy in the individual velocity components across all atmospheric stability regimes, and at the two different sites. The periods analyzed here are the same as in Fig. 1.

Figure 3 compares the empirically determined $p(k)$ with the best-fitted γ distribution (for $p(k)$ itself, not its variance components) and in a similar fashion the best-fitted log-normal distribution to the same data presented in Fig. 1. It is evident that the γ distribution describes $p(k)$ better than the alternative log-normal $p(k)$, consistent with the expectations proposed earlier. This finding is also suggestive that a Langevin equation recovering a γ $p(k)$ is superior to one recovering a log-normal distribution for k.

B. Gamma distribution prediction for k

Figure 4 shows predictions of γ_k and β_k from Eq. (8) when β_u and γ_u, β_v and γ_v, and β_w and γ_w are obtained by fitting separately a γ distribution to each u'^2, v'^2, and w'^2, compared against γ_k and β_k obtained by directly fitting a γ distribution to measured k (for each run at each site). The agreement is acceptable and suggests that the compound γ distribution for k is, in fact, the outcome of a super-position of independent γ fits to the squared anisotropic turbulent velocity components

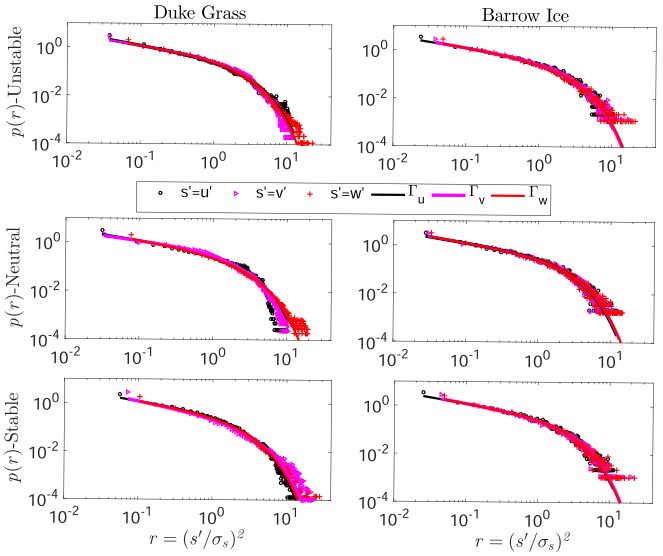

FIG. 2. The empirical distribution of $r = (s'/\sigma_s)^2$ for $s'^2 = u'^2$, $s'^2 = v'^2$, and $s'^2 = w'^2$ along with a fitted γ distribution for each velocity component. The γ fit was obtained using a maximum likelihood estimation.

(especially for neutral and mildly stable/unstable scenarios). While the probability law for $p(k)$ appears to be robust, the $\gamma_k \in [0.8, 1.8]$ is not constant and implies that $p(k)$ can be reduced to a near-exponential distribution at $\gamma_k = 1$ (a condition to be considered later on).

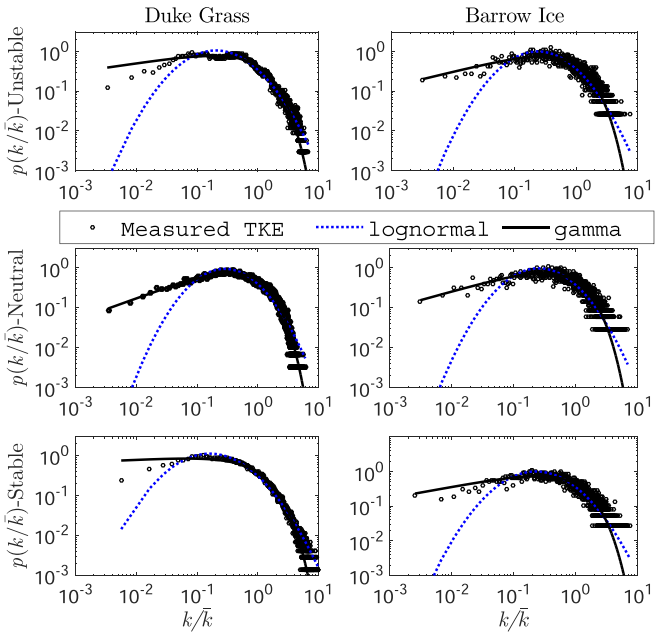

FIG. 3. A comparison between the empirically determined $p(k/\bar{k})$, a γ fit and a log-normal fit to $p(k/\bar{k})$ for the same runs featured in Figs. 1 and 2.

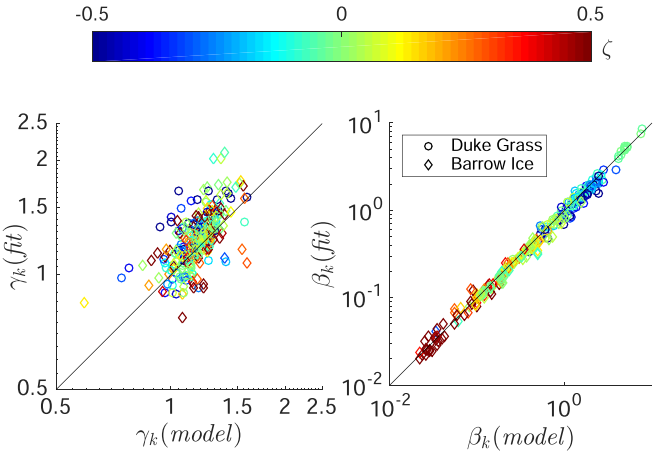

FIG. 4. The evaluation of Eq. (8) using individually determined β_u and γ_u, β_v and γ_v, and β_w and γ_w.

C. The Langevin equation

Having described the probability law for $p(k)$, the relaxation of TKE fluctuations to $\overline{k}$ are now considered. These relaxations are discussed in the context of the autocorrelation function shape. Figure 5 shows the measured $\rho_k(\tau)$ of k with time lags τ along with the approximation by an exponential model $\rho_k(\tau) = \exp(-\tau/\tau_k)$. The integral timescale ($= \tau_k$) is determined here in Fig. 5 by integrating the measured $\rho_k(\tau)$ up to the first zero-crossing from the measured k time series. The near-exponential decay at large lags is suggestive that a Langevin model with a linear drift (but a nonlinear diffusion term) may be plausible. The stationary continuously turbulent periods analyzed here are the same as those described in Fig. 1 for illustration.

Figure 6 shows—without loss of generality—sample trajectories of k computed using the Langevin Eq. (9) and measured $k/\overline{k}$, where the mean, variance, and integral timescale are based

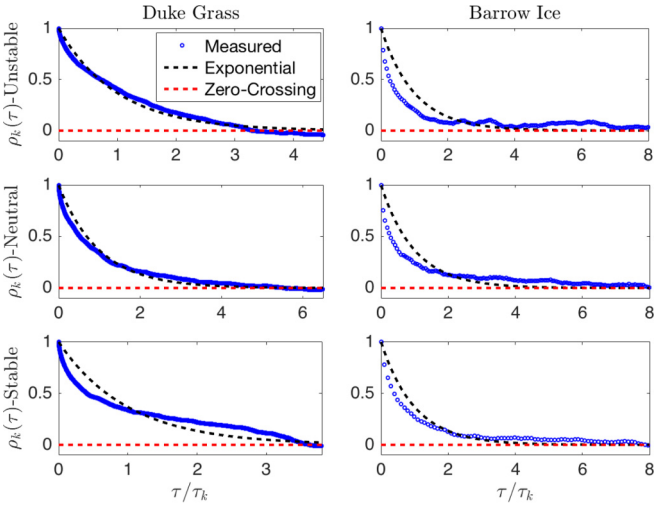

FIG. 5. The autocorrelation $\rho_k(\tau)$ as a function of normalized time lag τ/τ_k for the same runs featured in Fig. 1. The integral timescale of k ($= \tau_k$) was determined by integrating the measured $\rho_k(\tau)$ up to the first zero-crossing.

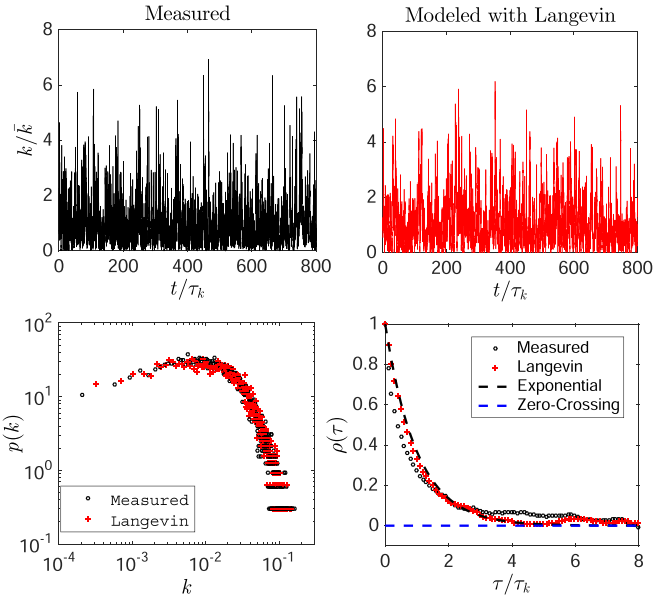

FIG. 6. The measured $k/\overline{k}$ (top left) and sample trajectories from the proposed Langevin equation of $k/\overline{k}$ (top right) with normalized time (τ_k). The comparison between measured and Langevin modeled $p(k)$ (bottom left) and their autocorrelation function $\rho(\tau)$ (bottom right) is also shown.

on the TKE of Barrow's stable ASL period in Fig. 1 (bottom right). The Langevin equation with a linear drift reproduces the main distributional and autocorrelation properties of measured k.

With the assumptions and simplifications leading to Eq. (9) supported by the experiments, the parameters of the Langevin equation are now discussed. The Langevin equation requires the external specification of $\overline{k}$, σ_k, and τ_k. A link between these three quantities and basic flow properties is now analyzed. Figure 7 shows the relation between $\overline{k}$ and u_*^2 and the variability σ_k versus $\overline{k}$. In ASL flows, the squared friction velocity (u_*^2) represents the kinematic ground shear stress and forms a logical basis for normalizing all second-order velocity statistics, including k. The data suggests that σ_k is proportional to $\overline{k}$, which is reasonably predicted from u_*^2. Unstable and stable data points lie off the neutral-limit line (discussed below) as expected. The coefficient of variation $CV_k = \sigma_k/\overline{k} \approx 1.1$. In a near-neutral ASL, it is usually observed that $A_u = \sigma_u/u_* \approx 2.7$, $A_v = \sigma_v/u_* \approx 2.4$, and $A_w = \sigma_w/u_* \approx 1.3$ [36], which then yields $\overline{k}/u_*^2 = A_k = (1/2)(2.7^2 + 2.1^2 + 1.3^2) = 7.4$. This estimate (i.e., $\overline{k} = A_k u_*^2$, $A_k = 7.4$) is in agreement with the measurements here as depicted in Fig. 7.

The parameters of the γ distribution γ_k and β_k can also directly inferred from u_*. Using a moment matching approach, $\overline{k} = A_k u_*^2 = \gamma_k/\beta_k$ and $\sigma_k^2 = (CV_k A_k u_*^2)^2 = \gamma_k/\beta_k^2$, yielding $\beta_k = (CV_k^2 A_k u_*^2)^{-1}$ as well as $\gamma_k = (CV_k)^{-2}$ independent of u_*. When $CV_k = 1$, $\gamma_k = 1$ and the γ distribution for $p(k)$ reduces to an exponential. That is, u_* and a specification of CV_k suffices to describe the parameters of the Langevin model for k as well as the parameters of the γ-distributed $p(k)$. When $CV_k < 1$, $\gamma_k > 1$, and conversely. The γ_k reported in Fig. 4 ranges between 0.8 and 1.8, resulting in a concomitant range in CV_k between 1.1 to 0.74. This CV_k range is narrow and suggestive that σ_k can be pragmatically inferred from $\overline{k}$ in ASL flows. To summarize, the friction velocity u_* (or equivalently the ground-shear stress) describes two of the three parameters in the Langevin equation for k. The remaining parameter is τ_k, which also requires characterization.

After experimenting with various choices of timescales in the stationary continuously turbulent periods, an advective timescale formed by z and $\Delta\overline{U} = \overline{U}(z) - \overline{U}(z_0)$ that represents the momentum deficit at height z relative to the surface roughness height z_0, hereafter labeled as $\tau_a = (\kappa z/\Delta\overline{U})$ appears to provide the best description to the variations in the measured decorrelation timescale.

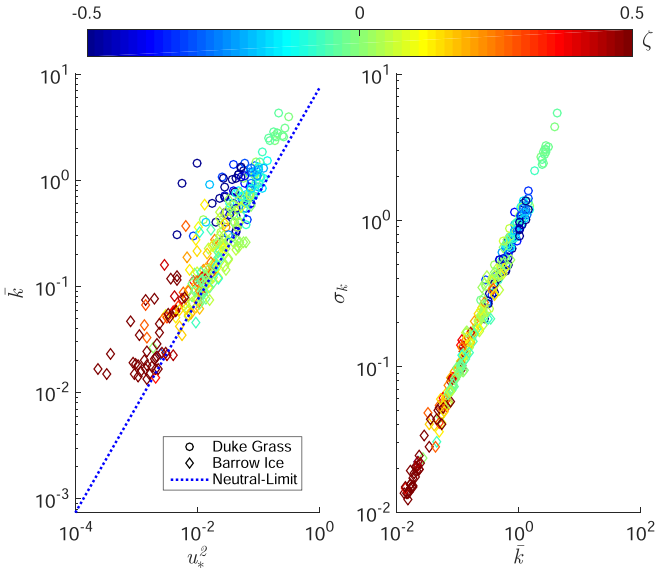

FIG. 7. The measured $\overline{k}$ versus measured u_* (left, neutral-limit has a slope $A_k = 7.4$) and $\overline{k}$ versus the variability in k ($=\sigma_k$) (right). Note that $\overline{k} \sim u_*^2$ and $\sigma_k \sim \overline{k}$ implies a $\sigma_k \sim u_*^2$.

Figure 8 shows the relation between τ_k determined here from the exponential decay of the auto-correlation function during its first e-folding "τ_e :e-folding time" and τ_a at both sites and under all atmospheric stability conditions. Ideally, τ_k would determined from the decay up to the first zero-crossing of the autocorrelation function as we have done till this point in the paper, but this new calculation that focuses on the first e-folding, $\tau_k \sim \tau_e$, is found to better characterize the integral timescale of most relevance to the TKE dynamics by eliminating longer timescales associated with weakly-energetic eddies at higher lags. It is also better related to τ_a and yields smaller model errors as we will later show. The good relation between τ_k and τ_a underlines the fact that fixed sensors, under relatively high wind conditions when the turbulence field is approximately frozen, measure the length of the eddies. The decay of the correlation in k can therefore be linked to the speed of advection of the eddies past the sensor. It is also clear from Fig. 8 that τ_k is greater than τ_a especially for the Duke site, and such overestimation might be attributed to the way τ_k is determined. The role

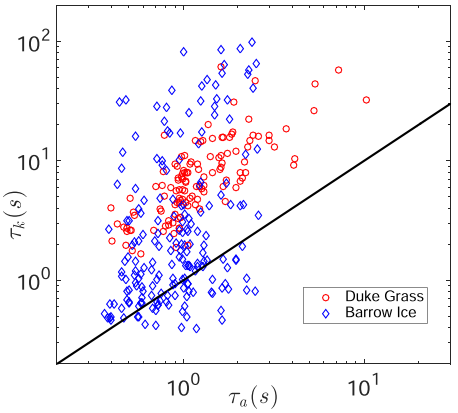

FIG. 8. The variations in measured τ_k versus measured τ_a. The solid black line is the one-to-one reference.

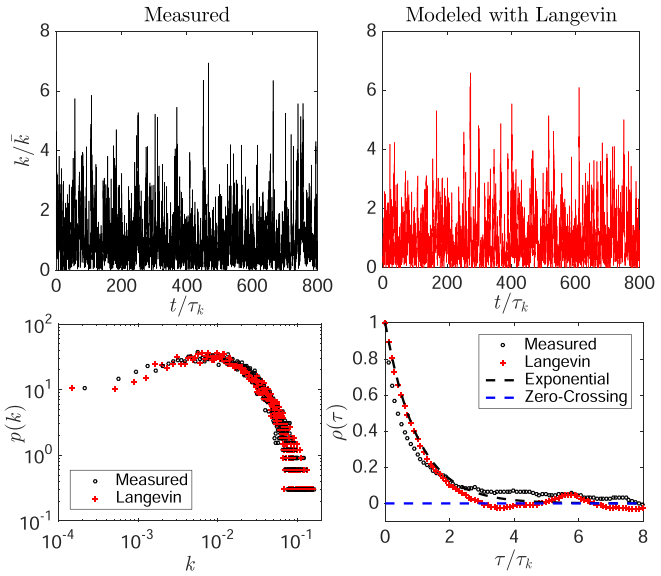

FIG. 9. The measured $k/\overline{k}$ (top left) and sample trajectories from the proposed Langevin model of $k/\overline{k}$ (top right) with normalized time (τ_k). The comparison between measured and Langevin modeled $p(k)$ (bottom left) and their autocorrelation function $\rho(\tau)$ (bottom right) is also shown.

of stability in modulating the drop of the autocorrelation function when estimating τ_k at both sites warrants further inquiry, but for simplicity it is assumed here that $\tau_k \sim \tau_e$, independent of stability. As depicted in the measured autocorrelation plots of Figs. 6 and 9, the sustained mild nonstationarity at higher lags might justify the long τ_k relative to τ_a as the latter describes the measured $p(k)$ rather well (illustrated later). With that, Eq. (10) can now be expressed as

$$dk \approx -(k - c_2 u_*^2)\frac{dt}{c_3\tau_a} + \sqrt{\left(\frac{2(c_1 u_*^2)^2 c_2 u_*^2 k}{c_3\tau_a}\right)}d\omega, \tag{11}$$

where the approximations $\sigma_m \approx c_1 u_*^2$, $\overline{k}_m \approx c_2 u_*^2$, and $\tau_m \approx c_3\tau_a$ are used. From Fig. 8, it is noted that the quantitative agreement between τ_k and τ_a leaves much to be desired, and the trends appear to be site-specific and stability dependent. However, τ_a is found to be the best timescale that correlates with τ_k, and approximating $\tau_m \approx c_3\tau_a$ here means that all time variables could be scaled with respect to τ_m or τ_k (as shown in the modeled plots). Later analysis on the exponential decaying autocorrelation functions using a constant relaxation timescale reveals that such assumption warrant further inquiry.

Figure 9 shows once again—without loss of generality—sample trajectories of k computed using the modeled Langevin Eq. (10) or Eq. (11) and measured $k/\overline{k}$ for the same period considered in Fig. 6, where the mean, variance, and integral timescale are all modeled and determined from u_* and $\Delta\overline{U}$. This modeled Langevin equation with a linear drift reproduces the main distributional and autocorrelation properties of the measured k as faithfully as the results in Fig. 6. It will be shown in the discussion that this Langevin model with the introduced modeled parameters described in Eqs. (10) and (11) in fact captures the simultaneous description of the distributional and autocorrelation properties of measured k when compared to Eq. (9). It even improves the agreement statistics if the timescale to be modeled is solely based on $\tau_m \approx \tau_a$.

V. DISCUSSION

Returning to Eqs. (9) and (10), we now ask how well the two Langevin equations reproduce the measured $p(k)$ and how well a relaxation to $\overline{k}$ is captured by an exponential model for the

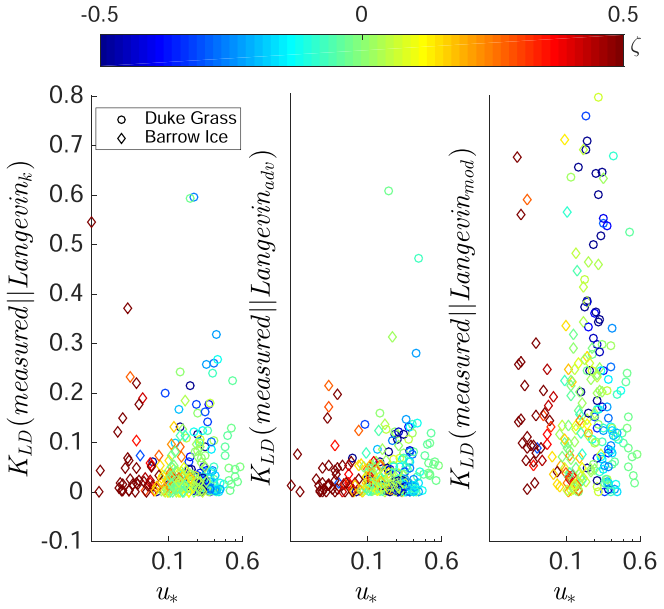

FIG. 10. The K_{LD} between measured $p(k)$ and theoretical $p(k)_{Lk}$ based on τ_k (left), the K_{LD} between measured $p(k)$ and proposed $p(k)_{Lm}$ based on τ_a only (middle), and the K_{LD} between measured $p(k)$ and proposed $p(k)_{Lm}$ based on σ_m, $\overline{k}_m$, and τ_a (right). The K_{LD} metrics between measured $p(k)$ versus predicted $p(k)_{Lk}$ and $p(k)_{Lm}$ based on time series from Eqs. (9) and (10), respectively, are scattered with respect to u_* and ζ.

autocorrelation function. To answer the first question, the time evolution of k across all periods is modeled using Eqs. (9) and (10) and compared separately with the measured $p(k)$. To assess this comparison quantitatively, the KullbackLeibler divergence (also called relative entropy)—which is a distance measure of how one probability distribution deviates from a reference probability distribution—is used [37]. The Kullback-Leibler divergence metric [38] is given by Eqs. (12) and (13), where $\Gamma(\gamma_{km}, \beta_{km})$ represents ("measured/analytical" distribution), $\Gamma(\gamma_{Lk}, \beta_{Lk})$ represents ["Langevin modeled/approximating" distribution based on Eq. (9)], and $\Gamma(\gamma_{Lm}, \beta_{Lm})$ represents ["Langevin modeled/approximating" distribution based on Eq. (10) or Eq. (11)]. For clarity, these measures are listed as

$$K_{\mathrm{LD}}(\mathrm{measured}||\mathrm{Langevin}_k) = (\gamma_{km} - \gamma_{Lk})\psi(\gamma_{km}) + \log\left(\frac{\Gamma(\gamma_{Lk})}{\Gamma(\gamma_{km})}\right) + \gamma_{Lk}\left[\log\left(\frac{\beta_{km}}{\beta_{Lk}}\right)\right] + \gamma_{km}\frac{\beta_{Lk} - \beta_{km}}{\beta_{km}}, \tag{12}$$

and

$$K_{\mathrm{LD}}(\mathrm{measured}||\mathrm{Langevin}_m) = (\gamma_{km} - \gamma_{Lm})\psi(\gamma_{km}) + \log\left(\frac{\Gamma(\gamma_{Lm})}{\Gamma(\gamma_{km})}\right) + \gamma_{Lm}\left[\log\left(\frac{\beta_{km}}{\beta_{Lm}}\right)\right] + \gamma_{km}\frac{\beta_{Lm} - \beta_{km}}{\beta_{km}}, \tag{13}$$

A Kullback-Leibler divergence of 0 indicates that the two distributions being compared are identical (zero-distance between them). Figure 10 shows that the K_{LD} metric of measured $p(k)$ versus predictions of $p(k)$ from time series runs using Eqs. (9) and (10) are not highly sensitive to u_* and ζ. Equation (11) captures the predicted distributions where the K_{LD} is still minimal as

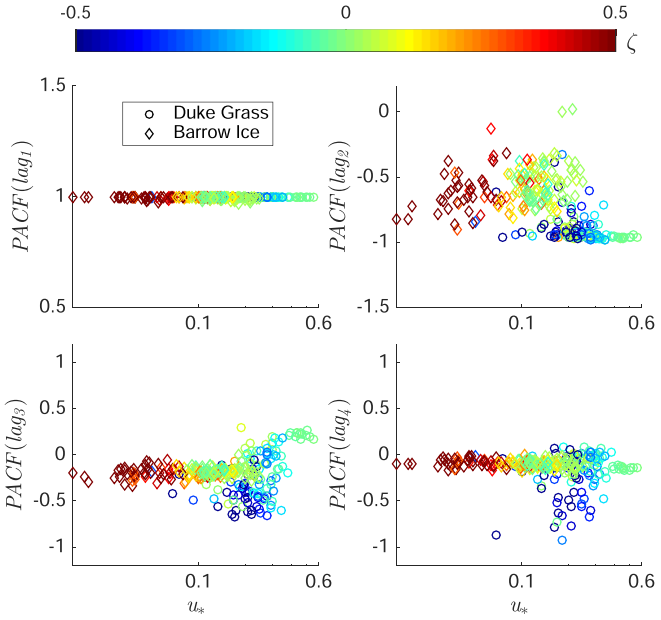

FIG. 11. PACF(lag_1) (top left), PACF(lag_2) (top right), PACF(lag_3) (bottom left), and PACF(lag_4) (bottom right) are scattered with respect to u_* and ζ.

illustrated in Fig. 10 (right), but it under-performs for extreme stable ($\zeta > 0$) or extreme unstable scenarios ($\zeta < 0$) where the K_{LD} increases significantly. Surprisingly, Eq. (9) (with modeling only the timescale $\tau_k \approx \tau_a$) outperforms Eq. (9) (with modeling only the timescale $\tau_k \approx \tau_e$), where K_{LD} is reduced significantly as illustrated in Fig. 10 (middle). This comparison may indicate that τ_a is a better measure of linear relaxation than estimates of τ_k based on one exponential decay of the measured autocorrelation function, at least in this context. This is clear in the exponential model with τ_k and τ_a that overpredicts the measured autocorrelation function at small lags but underpredicts the measured autocorrelation function at large lags (Figs. 6 and 9). The reason the Langevin model with τ_a yields smaller K_{LD} compared to the case with $\tau_k \approx \tau_e$ is that τ_a is smaller than τ_k for most of the periods. This is justified in the Langevin model where the nonlinear diffusion term (that scales with $\tau^{-1/2}$) will lead to faster decorrelation (consistent with measured autocorrelation), but the final decay phases at large lags of the measured autocorrelation is dictated by the drift (think of mild nonstationarity) which then becomes large (again consistent with the data).

To answer the second question, the sample partial autocorrelation function (PACF) is tested at the first 4 lags [39]. The PACF is used to determine the complexity (or order) of an equivalent autoregressive model that best describes the autocorrelation function of data, i.e., the partial autocorrelation function at a set lag is the correlation that results after removing the effect of any correlations due to terms at shorter lags. It is entirely determined from the shape of the autocorrelation function. The approach used here solves the so-called Yule-Walker equations described elsewhere [40,41]. A p-order autoregressive model for variable $\vartheta(t)$ takes the form

$$\vartheta(t) = a_1\vartheta(t-1) + a_2\vartheta(t-2) + \cdots + a_p\vartheta(t-p) + \epsilon_r(t), \tag{14}$$

where $\epsilon_r(t)$ is a white-noise process with an arbitrary variance (the noise term), $a_1, a_2, \ldots$ are the coefficients of the autoregressive process that can be inferred from the PACF, and $t-1, t-2$, etc... are lag-1, lag-2, and so forth. First-order autoregressive models are associated with exponentially decaying autocorrelation functions where the PACF is only finite at lag 1 and insignificant everywhere else. Figure 11 shows that PACF(lag_1) dominates the rest of the lags, meaning an exponential decay

of the autocorrelation using a constant relaxation timescale is a leading-order estimate. However, PACF(lag_2) and PACF(lag_3) are, by no means, insignificant. The PACF(lag_2) shows less variability for the unstable data points unlike the case for the stable ones; however, PACF(lag_3) shows less variability for the stable data points unlike the case for the unstable ones. The PACF(lag_4) exhibits a similar behavior as PACF(lag_3), but the stable data points are consistently zero now. Thus, nonlinear relaxation or deviations from exponential autocorrelation function decay warrant further inquiry. How to accommodate these features in a nonlinear drift term is a topic better kept for future work

VI. SUMMARY AND CONCLUSIONS

The probability density function of k, $p(k)$, in a diabatic atmospheric surface layer is analyzed. When the component-wise velocity fluctuations are Gaussian and their squares are un-correlated with each other, $p(k)$ follows a χ-squared distribution as expected. Deviations from Gaussian velocity components revise the χ-squared to a γ-distributed $p(k)$. Experiments support the γ-distributed $p(k)$ with shape parameters bounded between 0.8 and 1.8. Variations in k around $\overline{k}$ can be represented by a Langevin equation with a linear drift characterized by a relaxation time τ_k and a nonlinear diffusion term characterized by τ_k, $\overline{k}$ and the standard deviation of k, σ_k.

At two sites that differ in surface cover type and homogeneity, it was shown that $\overline{k}$ and σ_k scale primarily with the friction velocity u_*. The τ_k is best approximated by an advection time $\kappa z/\Delta\overline{U}$. The parameters of the Langevin equation are not explicitly sensitive to the range of atmospheric stability ζ observed in the experiments except for extreme stable/unstable scenarios. Hence, exploring other sites with a wider range of synoptic conditions and stabilities is needed for a more conclusive analysis of the role of buoyancy. The $\Delta\overline{U}$ needed in the integral timescale does vary with atmospheric stability ζ. When $\overline{k}$, σ_k, and τ_k are modeled from $\Delta\overline{U}$ and u_*, the Langevin equation describes the stationary $p(k)$ reasonably at both sites. This was concluded with the aid of the Kullback-Leibler divergence metric test, which was shown to be acceptable when applied to all the periods at the two sites. When τ_k is solely modeled, the Kullback-Leibler divergence metric was almost null across all stabilities.

Analysis of the partial autocorrelation function (PACF) suggests that lag_1 remains the most significant (i.e., exponential decay). Numerous runs exhibit nontrivial PACF at lags up to 4, implying nonexponential decay in the autocorrelation function cannot be entirely ignored for all runs. Such adjustments need not revise the linearity of the drift term and can be accommodated by assuming a relaxation timescale that is not constant, but rather time dependent. A nonconstant relaxation time is one possibility to bridge the Langevin equation for k here and arguments employed in super-statistics. For example, it has been known for quite some time now that a system with a micro-state V evolving as

$$\frac{dV}{dt} = -\gamma_s V + \sigma_s d\omega, \tag{15}$$

and with a nonconstant $\beta_s = \gamma/\sigma^2$ sampled from a certain class of probability density functions $p(\beta_s)$ result in an entropy that does not abide by the standard BoltzmannGibbs form (i.e., Tsallis) as discussed elsewhere [9]. Returning to the Langevin model proposed for k, a τ_k that is itself derived from a distribution can also be interpreted in a similar manner.

Future work will explore $p(k)$ in the roughness sublayer of urban and vegetated canopies alike to assess whether there is a signature of roughness on $\overline{k}$, σ_k, and τ_k. Also, the presence of patchy turbulence regimes expected in extremely stably stratified flow characterized by a flux Richardson number $Ri_f > 0.21$ are conjectured to introduce substantial deviations from a γ distributed $p(k)$. Such patchiness in turbulence resembles an on-off TKE dissipation rate time series and may shift $p(k)$ to a log-normal shape given the large sporadic 'bursts' in k dominating such stability regimes.

ACKNOWLEDGMENTS

M.A. and E.B.Z. are supported by the Cooperative Institute for Modeling the Earth System at Princeton University under Award No. NA18OAR4320123 from the National Oceanic and Atmospheric Administration, and by the Andlinger Center for Energy and the Environment at Princeton University. G.K. acknowledges support from the U.S. National Science Foundation (Grants No. NSF-AGS-1644382, NSF-AGS-2028633 and No. NSF-IOS-1754893), as well as Princeton Universitys Metropolis Project for partial support during a sabbatical leave at Princeton in 2020. J.D.F. acknowledges the support provided by the National Science Foundation to complete the PHOXMELT field studies (Grant No. PLR-1417914) to collect the data. We thank K. Pratt, P. Shepson, Sham Thanekar, and J.Ruiz-Plancart for their contributions to obtaining the turbulence data set at Utqiagvik, Alaska during 2016 field campaign.

[1] V.-M. Kumer, J. Reuder, M. Dorninger, R. Zauner, and V. Grubišić, Turbulent kinetic energy estimates from profiling wind LiDAR measurements and their potential for wind energy applications, Renew. Energy **99**, 898 (2016).

[2] M. Llaguno-Munitxa and E. Bou-Zeid, Shaping buildings to promote street ventilation: A large-eddy simulation study, Urban Clim. **26**, 76 (2018).

[3] M. Momen and E. Bou-Zeid, Mean and turbulence dynamics in unsteady Ekman boundary layers, J. Fluid Mech. **816**, 209 (2017).

[4] G. L. Mellor and T. Yamada, Development of a turbulence closure model for geophysical fluid problems, Rev. Geophys. **20**, 851 (1982).

[5] M. Wichmann and E. Schaller, On the determination of the closure parameters in higher-order closure models, Boundary-Layer Meteorol. **37**, 323 (1986).

[6] R. van Hout, M. Chamecki, G. Brush, J. Katz, and M. Parlange, The influence of local meteorological conditions on the circadian rhythm of corn (Zea mays L.) pollen emission, Agr. Forest Meteorol. **148**, 1078 (2008).

[7] G. Pazos, D. Greene, G. Katul, M. Bertiller, and M. Soons, Seed dispersal by wind: Towards a conceptual framework of seed abscission and its contribution to long-distance dispersal, J. Ecol. **101**, 889 (2013).

[8] J. Treep, M. de Jager, L. S. Kuiper, T. Duman, G. G. Katul, and M. B. Soons, Costs and benefits of nonrandom seed release for long-distance dispersal in wind-dispersed plant species, Oikos **127**, 1330 (2018).

[9] C. Beck, Superstatistics in hydrodynamic turbulence, Physica D **193**, 195 (2004).

[10] C. Beck, E. G. D. Cohen, and H. L. Swinney, From time series to superstatistics, Phys. Rev. E **72**, 056133 (2005).

[11] H. Touchette and C. Beck, Asymptotics of superstatistics, Phys. Rev. E **71**, 016131 (2005).

[12] L. Mahrt, Nocturnal boundary-layer regimes, Boundary-Layer Meteorol. **88**, 255 (1998).

[13] L. Mahrt, Stratified atmospheric boundary layers, Boundary-Layer Meteorol. **90**, 375 (1999).

[14] J. Sun, D. H. Lenschow, S. P. Burns, R. M. Banta, R. K. Newsom, R. Coulter, S. Frasier, T. Ince, C. Nappo, B. B. Balsley *et al.*, Atmospheric disturbances that generate intermittent turbulence in nocturnal boundary layers, Boundary-Layer Meteorol. **110**, 255 (2004).

[15] J. Sun, L. Mahrt, R. M. Banta, and Y. L. Pichugina, Turbulence regimes and turbulence intermittency in the stable boundary layer during cases-99, J. Atmos. Sci. **69**, 338 (2012).

[16] G. G. Katul, A. Porporato, S. Shah, and E. Bou-Zeid, Two phenomenological constants explain similarity laws in stably stratified turbulence, Phys. Rev. E **89**, 023007 (2014).

[17] B. Van de Wiel, A. Moene, O. Hartogensis, H. De Bruin, and A. Holtslag, Intermittent turbulence in the stable boundary layer over land. Part III: A classification for observations during cases-99, J. Atmos. Sci. **60**, 2509 (2003).

[18] N. Vercauteren and R. Klein, A clustering method to characterize intermittent bursts of turbulence and interaction with submesomotions in the stable boundary layer, J. Atmos. Sci. **72**, 1504 (2015).

[19] I. G. van Hooijdonk, H. J. Clercx, C. Ansorge, A. F. Moene, and B. J. van de Wiel, Parameters for the collapse of turbulence in the stratified plane Couette flow, J. Atmos. Sci. **75**, 3211 (2018).
[20] C. Ansorge and J. P. Mellado, Global intermittency and collapsing turbulence in the stratified planetary boundary layer, Boundary-Layer Meteorol. **153**, 89 (2014).
[21] C. Ansorge and J. P. Mellado, Analyses of external and global intermittency in the logarithmic layer of ekman flow, J. Fluid Mech. **805**, 611 (2016).
[22] O. C. Acevedo and D. R. Fitzjarrald, In the core of the night-effects of intermittent mixing on a horizontally heterogeneous surface, Boundary-Layer Meteorol. **106**, 1 (2003).
[23] A. Monin and A. Obukhov, Basic laws of turbulent mixing in the surface layer of the atmosphere, Dokl. Akad. Nauk SSSR **24**, 163 (1954).
[24] G. G. Katul, L. Mahrt, D. Poggi, and C. Sanz, One-and two-equation models for canopy turbulence, Boundary-Layer Meteorol. **113**, 81 (2004).
[25] A. Obukhov, Turbulence in an atmosphere with a nonuniform temperature, Boundary-Layer Meteorol. **2**, 7 (1971).
[26] J. Ruiz-Plancarte, J. Fuentes and S. Thanekar, Air turbulence data over the Barrow Environmental Observatory, Alaska, Arctic Data Center, (2019) doi:10.18739/A2R20RW3W.
[27] G. Katul, C.-I. Hsieh, and J. Sigmon, Energy-inertial scale interactions for velocity and temperature in the unstable atmospheric surface layer, Boundary-Layer Meteorol. **82**, 49 (1997).
[28] C. Chu, M. Parlange, G. Katul, and J. Albertson, Probability density functions of turbulent velocity and temperature in the atmospheric surface layer, Water Resour. Res. **32**, 1681 (1996).
[29] H. Nakagawa and I. Nezu, Prediction of the contributions to the Reynolds stress from bursting events in open-channel flows, J. Fluid Mech. **80**, 99 (1977).
[30] D. Poggi, A. Porporato, L. Ridolfi, G. Katul, and J. Albertson, The effect of vegetation density on canopy sublayer turbulence, Boundary-Layer Meteorol. **111**, 565 (2004).
[31] M. Raupach, Conditional statistics of Reynolds stress in rough-wall and smooth-wall turbulent boundary layers, J. Fluid Mech. **108**, 363 (1981).
[32] F. Satterthwaite, An approximate distribution of estimates of variance components, Biometrics **2**, 110 (1946).
[33] B. Welch, The generalization of student's' problem when several different population variances are involved, Biometrika **34**, 28 (1947).
[34] S. Pope, *Turbulent Flows* (Cambridge University Press, Cambridge, MA, 2000) p. 771.
[35] T. Duman, A. Trakhtenbrot, D. Poggi, M. Cassiani, and G. Katul, Dissipation intermittency increases long-distance dispersal of heavy particles in the canopy sublayer, Boundary-Layer Meteorol. **159**, 41 (2016).
[36] R. B. Stull, *An Introduction to Boundary Layer Meteorology* (Springer Science & Business Media, Berlin, 1988), Vol. 13.
[37] S. Kullback and R. Leibler, On Information and sufficiency, Ann. Math. Stat. **22**, 79 (1951).
[38] J. Soch and C. Allefeld, Kullback-Leibler divergence for the normal-gamma distribution, arXiv:1611.01437 (2016).
[39] G. E. Box, G. M. Jenkins, G. C. Reinsel, and G. M. Ljung, *Time Series Analysis: Forecasting and Control* (John Wiley & Sons, New York, 2015).
[40] G. Udny Yule, On a method of investigating periodicities in disturbed series, with special reference to Wolfer's sunspot numbers, RSPTA **226**, 267 (1927).
[41] G. T. Walker, On periodicity in series of related terms, Proc. R. Soc. London **131**, 518 (1931).